Angewandte Chemie International Edition

Angewandte International Edition Chemie

How to cite: *Angew. Chem. Int. Ed.* **2026**, e3640627
doi.org/10.1002/anie.3640627

RESEARCH ARTICLE OPEN ACCESS

Bio-Propelled Stomatocyte Nanomotors with Glutathione-Responsiveness for Osteoarthritis Treatment

Jianhong Wang[1] | Mengsi Zhan[2] | Hanglong Wu[1] | Maarten Bransen[3] | Ioanna Balmpouzi[1] | Xianwen Lou[1] | Junjie Liu[4] | Nina Wang[2] | Zhiqiang Wang[2] | Heiner Friedrich[3] | Jingxin Shao[1] | Jan C. M. van Hest[1] | Xiangyang Shi[2]

[1]Bio-Organic Chemistry, Department of Biomedical Engineering, Institute For Complex Molecular Systems (ICMS), Eindhoven University of Technology, Eindhoven, The Netherlands | [2]State Key Laboratory of Advanced Fiber Polymer Materials, Shanghai Engineering Research Center of Nano-Biomaterials and Regenerative Medicine, College of Biological Science and Medical Engineering, Donghua University, Shanghai, P. R. China | [3]Center For Multiscale Electron Microscopy, Department of Chemical Engineering and Chemistry, Eindhoven University of Technology, Eindhoven, The Netherlands | [4]DWI-Leibniz-Institute For Interactive Materials, Institute For Technical and Macromolecular Chemistry, RWTH Aachen University, Aachen, Germany

Correspondence: Jianhong Wang (jianhong.wang@dpag.ox.ac.uk) | Jingxin Shao (j.shao@tue.nl) | Jan C. M. van Hest (j.c.m.v.hest@tue.nl) | Xiangyang Shi (xshi@dhu.edu.cn)

Received: 6 December 2025 | **Revised:** 8 April 2026 | **Accepted:** 11 April 2026

Keywords: deep penetration | enhanced cell uptake | nanomotors | osteoarthritis treatment | self-actuation

ABSTRACT

Pharmacological intervention is a primary therapeutic strategy for Osteoarthritis (OA), however, improving the bioavailability of therapeutic agents remains a significant challenge. In this study, we developed oxygen-propelled, glutathione (GSH)-responsive stomatocyte nanomotors (MTX/MnO_2-GSH-stomatocytes) for osteoarthritis (OA) treatment. First, polymersomes were assembled composed of block copolymers containing a GSH-cleavable disulfide linker, which were loaded with the therapeutic agent methotrexate (MTX) into their hydrophilic domain. Upon dialysis-induced shape change bowl shaped stomatocytes were formed with manganese dioxide (MnO_2) particles encapsulated into the nanocavity with high loading efficiency. Within the OA microenvironment, MnO_2 decomposed the inflammatory hydrogen peroxide (H_2O_2), generating an O_2 gradient that propelled the nanomotors and enabled chemotactic movement for targeted cargo delivery. Meanwhile, after cellular uptake elevated GSH levels cleaved the disulfide linkers, inducing the collapse of the stomatocyte structure and the rapid release of MTX. The motility and targeted release behavior of the nanomotors were systematically evaluated both in vitro and in vivo. Experimental results demonstrated that these nanomotors effectively alleviated oxidative stress, inflammation, and cartilage degradation, while exhibiting negligible adverse effects. Overall, this study presents a promising GSH-responsive, nanomotor-based strategy for enhanced osteoarthritis therapy.

1 | Introduction

The field of synthetic nanomotors has attracted significant attention from a biomedical perspective. This is due to their ability to cross biological barriers through self-propelled motion using internal fuels or external energy sources [1–3]. Over the past decade, a wide range of nanomotors have been developed, including chemically-driven [4–6], light-driven [7–9], and magnetically-driven nanomotors [10–12]. Among these, chemically-driven nanomotors utilize biocompatible and

Jianhong Wang and Mengsi Zhan contributed equally to this work.

bioavailable fuels. These fuels generate local concentration gradients that induce autonomous movement [13, 14]. Such fuels are often endogenous by-products of pathological tissues or biological processes. For instance, tumor and osteoarthritic (OA) microenvironments exhibit elevated concentrations of hydrogen peroxide (H_2O_2) and glucose, while urea levels in the bladder can reach up to 300 mM [15, 16]. Several catalyst-mediated nanomotors have been reported that can autonomously move in biofuels-rich environments through catalytic reactions. For example, Sanchez et al. developed urease-powered nanobots by asymmetrically grafting urease onto mesoporous silica surfaces [17]. This system exhibited strong chemotactic motion within a tumor-mimicking microenvironment and demonstrated efficient penetration both in vitro and in vivo. Similarly, Tu and coworkers designed an enzymatic hollow mesoporous nanomotor that enhanced diffusion within the joint cavity of a gout mouse model, resulting in improved therapeutic efficacy [18]. While these studies have demonstrated the propulsion capability to improve tissue accumulation and penetration, efficient release of therapeutic payloads at the target site remains a major challenge. This limitation affects overall drug utilization [19]. In particular, the therapeutic efficacy of OA treatment is often constrained by suboptimal drug utilization and inadequate accumulation at lesion sites. Therefore, the application of nanotechnology to enhance the bioavailability and targeted delivery of anti-inflammatory agents represents a promising therapeutic strategy.

In recent years, we have developed bowl-shaped polymersomes, known as stomatocytes, featuring an open neck and a nanocavity [20]. Polymeric stomatocytes were originally inspired by the cup-shaped morphology of red blood cells observed in hematology and were later engineered through controlled self-assembly processes [21, 22]. Their intrinsic hollow cavity enables the efficient encapsulation of functional cargo (e.g., catalysts and enzymes), thereby facilitating the development of nanoreactors and nanomotors [23–25]. These structures are composed of biodegradable poly(ethylene glycol)-b-poly(D,L-lactide) (PEG-PDLLA) copolymers or non-biodegradable [26]. Their asymmetric structure has been exploited to construct nanomotors by loading enzymes or catalysts into their nanocavities and depositing functional metal nanoparticles onto their surfaces [27–31]. To fulfill the purpose of in-site drug release, some work has been reported on incorporating responsive linkers into block polymers to form polymersomes [32–35]. However, these polymersomes were either non-biodegradable, restricted to spherical morphologies, or limited by lower responsive-copolymer ratios, which is unsatisfactory for further biomedical applications [36–38]. In addition, biodegradable responsive stomatocytes have predominantly been studied from a fundamental perspective, while in vivo applications across diverse disease contexts remain limited. Herein, we present glutathione (GSH)-responsive biodegradable stomatocyte nanomotors designed for active delivery of therapeutic cargo to osteoarthritic (OA) sites. The nanomotor was fabricated through three main steps (Figure 1): (1) formation of pure GSH-responsive stomatocytes via disulfide linkers mediated biodegradable copolymers of PEG-PDLLA; (2) loading of the therapeutic agent methotrexate (MTX) [39, 40] into the hydrophilic domain of the stomatocytes; and (3) encapsulation of oxygen-generating manganese dioxide (MnO_2) nanoparticles (NPs) within the stomatocyte nanocavity. Unlike conventional GSH-responsive polymers with GSH-responsive block copolymers, our nanomotors were self-assembled entirely from 100% GSH-responsive biodegradable block copolymers. This design ensures uniform responsiveness and improved degradation behavior.

The self-assembly and GSH-triggered dissociation behavior of the GSH-stomatocytes were thoroughly characterized using SEM and cryo-TEM. Controlled release of MTX, mediated by GSH responsive degradation, was demonstrated under simulated inflammatory conditions that mimic the OA microenvironment. To impart motility, MnO_2 NPs were subsequently incorporated into the stomatocyte's cavity via an in situ growth method, achieving a high loading efficiency of up to 80%. Motion studies revealed that the nanomotors exhibited self-propulsion and chemotactic behavior under OA-mimicking inflammatory conditions through decomposition of H_2O_2. Both in vitro and in vivo experiments demonstrated that MTX/MnO_2-GSH-stomatocyte nanomotors enhanced MTX bioavailability through GSH-mediated release, thereby improving therapeutic efficacy in OA. Collectively, this work introduces a promising strategy to enhance the therapeutic efficacy of MTX in the treatment of OA.

2 | Results and Discussion

To construct the nanomotor chassis and enable GSH-responsive release, biodegradable poly(ethylene glycol)-b-poly(D,L-lactide) (PEG-SS-PDLLA) block copolymers were synthesized. A disulfide linker was introduced between the hydrophilic PEG segment and the hydrophobic PDLLA domain to confer redox responsiveness. The disulfide bonds were designed to be cleaved under the high glutathione (GSH) concentrations typically found in the cytoplasm, thereby triggering stomatocyte disassembly and cargo release. The GSH-responsive block copolymers were synthesized following previously reported procedures [41, 42]. Briefly, 1,1'-carbonyldiimidazole (CDI)-mediated coupling was employed to introduce the disulfide linker onto PEG. The resulting PEG-CDI intermediate was subsequently reacted with 2,2-disulfanediyldiethanol to yield the PEG-SS-OH macroinitiator. The synthesis of these intermediates was confirmed by proton nuclear magnetic resonance (^{1}H NMR) spectroscopy, gel permeation chromatography (GPC), and matrix-assisted laser desorption/ionization-time-of-flight mass spectrometry (MALDI-ToF MS) (Figures S1–S7 and Table S2). The PEG-SS-PDLLA block copolymers were subsequently synthesized via ring-opening polymerization (ROP) [43]. The resulting copolymers were characterized by ^{1}H NMR and GPC analyses (Figures S6–S9 and Table S2). Stomatocytes were obtained through self-assembly of the PEG-SS-PDLLA block copolymers into spherical polymersomes, followed by dialysis against 50 mM NaCl solution to induce an osmotic-driven shape transformation. The morphology and hydrodynamic size of the stomatocytes were analyzed using dynamic light scattering (DLS), scanning electron microscopy (SEM), and cryogenic transmission electron microscopy (cryo-TEM). The images revealed a well-defined open-neck structure after shape transformation, with an average diameter of approximately 430 nm (Figure 2a), confirming the successful formation of GSH-responsive stomatocytes. MTX was subsequently loaded into the hydrophilic domain of the GSH-stomatocytes during the polymersome assembly process. UV-vis spectroscopy confirmed successful MTX encapsulation (Figure S10), and no significant morphological changes were

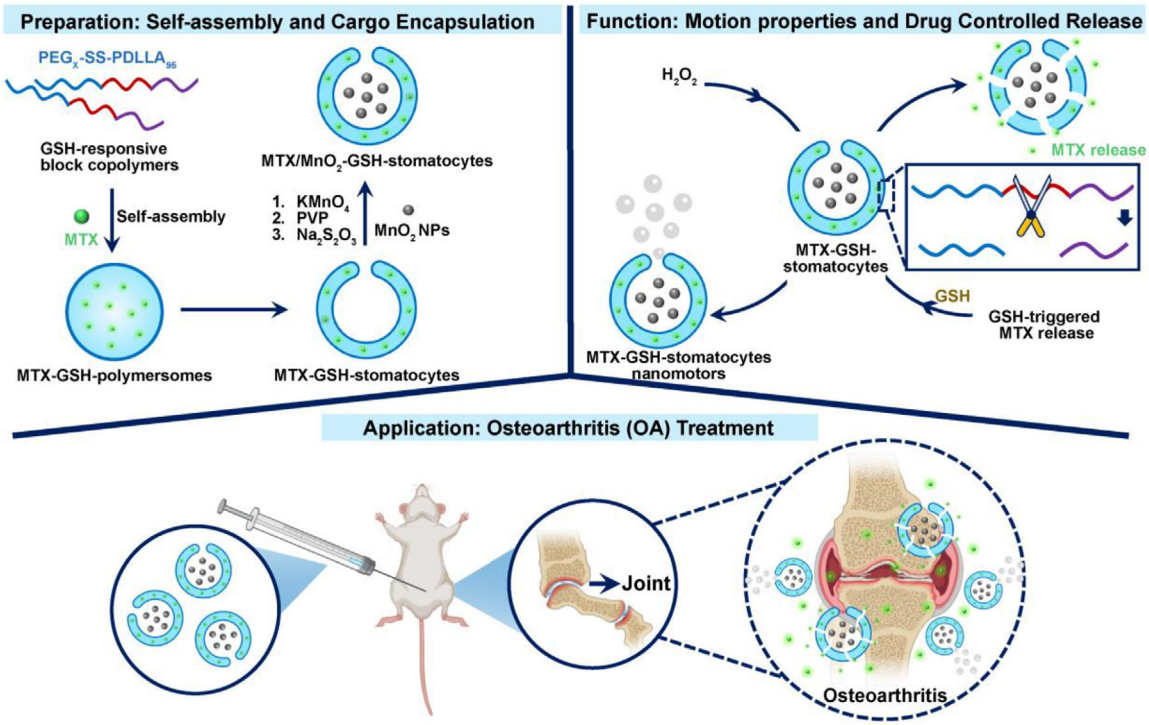

FIGURE 1 | Schematic illustration of the design and fabrication of O_2-powered GSH-stomatocyte nanomotors for OA treatment. Preparation of GSH-stomatocytes by introducing disulfide bonds into PEG-PDLLA copolymers, followed by loading of methotrexate (MTX) into the hydrophilic domain and in situ creation of MnO_2 nanoparticles within the stomatocyte nanocavity. Intra-articular delivery of O_2-powered GSH-stomatocyte nanomotors for the treatment of OA.

observed after loading (Figures 2b and S11). The loading efficiency (LE) and encapsulation efficiency (EE) of MTX, determined from the calibration curve (Figure S12), were 6.5% and 70%, respectively (Table S3). The colloidal stability of MTX-stomatocytes was evaluated under biological conditions in phosphate-buffered saline (PBS) and Dulbecco's Modified Eagle Medium (DMEM) over a 14-day period by monitoring changes in hydrodynamic diameter and polydispersity index (PDI). As shown in Figure S13, only minimal variations in hydrodynamic size and PDI were observed, indicating the good colloidal stability of the GSH-responsive stomatocytes. For comparison, MTX-loaded stomatocytes without GSH-responsive linkers were prepared as controls (Figure S14). The assembled GSH-stomatocytes were subsequently loaded with MnO_2 NPs using an improved in situ growth method, modified from our previously reported procedure [29, 44]. This strategy enabled the compartmentalization of MnO_2 NPs within the stomatocyte cavity, achieving a loading efficiency of 80% (Figure 2c). Cryo-TEM imaging confirmed the well-defined structure of the resulting hybrid stomatocytes. To examine the three-dimensional spatial distribution of MnO_2 NPs within the stomatocytes, cryo-electron tomography (cryo-ET) was performed on several MnO_2-GSH-stomatocytes (Figure 2d and Videos S1) [28, 29, 45] The cryo-ET analysis revealed that the MnO_2 NPs were encapsulated within the internal cavity of the stomatocytes. Additional cryo-ET datasets and corresponding tomographic reconstructions of other stomatocytes are provided in the (Figures S15 and S16).

The GSH-stomatocytes exhibited good colloidal stability under physiological conditions but rapidly collapsed and aggregated after 4 h of incubation with 10 mM GSH at room temperature (Figure 2e–g), indicating effective GSH-responsiveness. Cumulative release studies demonstrated that MTX release from the stomatocytes was markedly accelerated in the presence of 10 mM GSH (Figure 2h), compared to GSH-free conditions. This behavior can be attributed to the GSH-cleavable disulfide linker, which facilitates reductive de-crosslinking and structural degradation of the stomatocytes.

The constructed MnO_2-GSH-stomatocyte nanomotors exhibited autonomous motion in a disease-mimicking solution containing H_2O_2, driven by the MnO_2-mediated decomposition of H_2O_2 and the subsequent release of oxygen from the cavity of the stomatocytes. Nanoparticle tracking analysis (NTA) was performed to monitor the motion of the nanomotors and record their trajectories. The mean square displacements (MSDs) and velocities of the MnO_2-GSH-stomatocytes increased proportionally with the H_2O_2 concentration (Figure 3a). In the absence of H_2O_2, the MnO_2-GSH-stomatocyte nanomotors exhibited random Brownian motion, whereas the addition of H_2O_2 induced distinct self-propelled motion. The MnO_2-GSH-stomatocyte nanomotors exhibited velocities ranging from 2.3 ± 0.5 to 11.2 ± 1.9 μm/s (Figure 3b). Furthermore, the trajectory lengths of the MnO_2-GSH-stomatocyte nanomotors increased markedly with rising H_2O_2 concentrations, indicating that higher oxygen generation enhanced the driving force (Figure 3c). Given the presence of an H_2O_2 concentration gradient in the OA microenvironment, we next investigated if such gradient could be employed to induce chemotactic behavior into the MnO_2-GSH-stomatocyte nanomotors. A single-channel slide was used for in vitro chemotaxis analysis. To

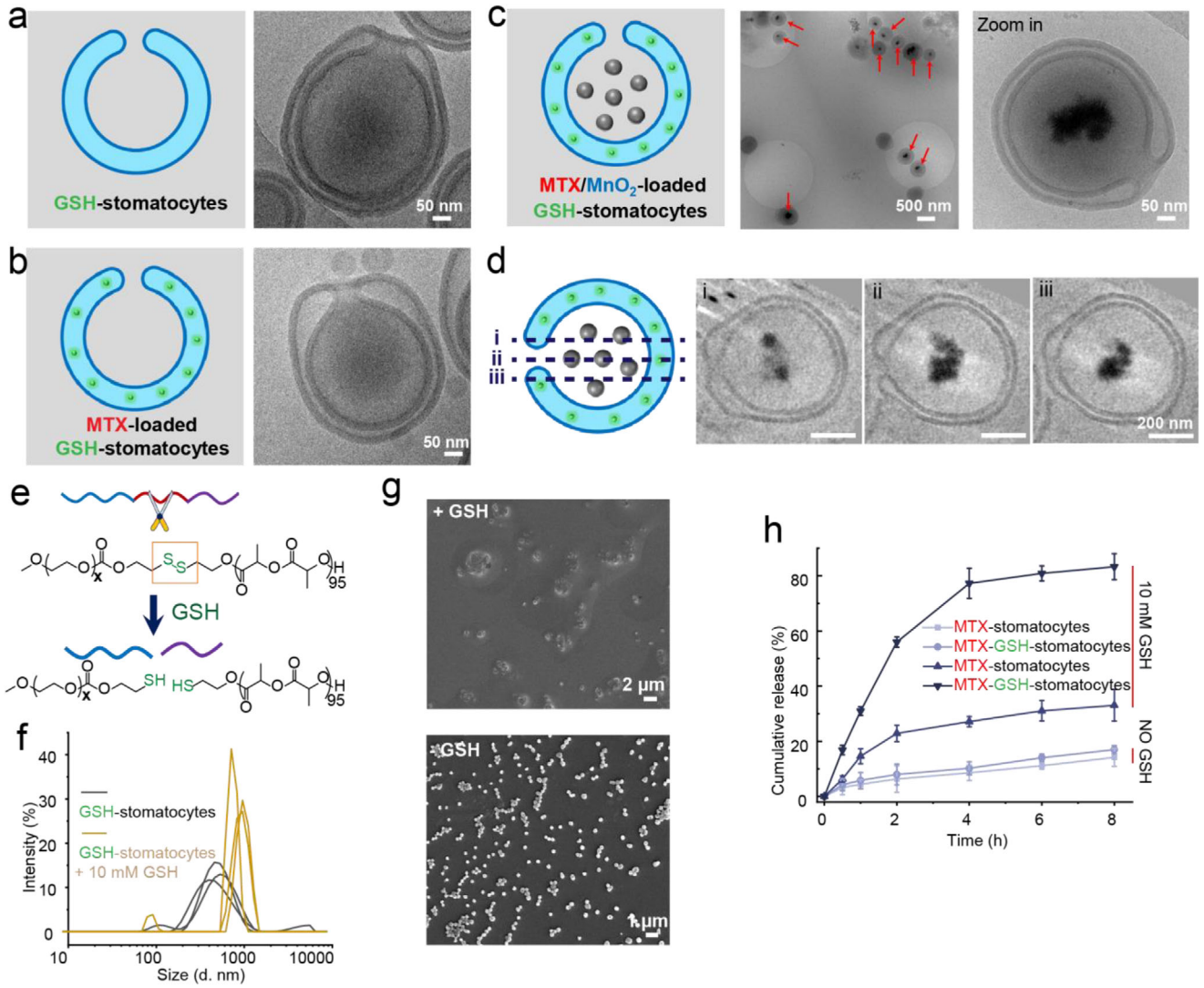

FIGURE 2 | Preparation and characterization of MTX/MnO_2-loaded GSH-stomatocyte nanomotors (MTX/MnO_2-GSH-stomatocytes). (a) Schematic illustration (left) and cryo-TEM image (right) of GSH-stomatocytes. Scale bar = 50 nm. (b) Schematic illustration (left) and cryo-TEM image (right) of MTX loaded GSH-stomatocytes (MTX-GSH-stomatocytes). Scale bar = 50 nm. (c) Schematic illustration (left) and cryo-TEM images (right) of MnO_2 and MTX loaded GSH-stomatocytes (MTX/MnO_2-GSH-stomatocytes). Scale bar = 500 nm (left) / 50 nm (right). (d) Cryo-electron tomography (cryo-ET) images of an MTX/MnO_2-GSH-stomatocyte. Cross-sectional slices (i–iii) acquired from different regions reveal that MnO_2 nanoparticles are encapsulated within the cavity near the opening of the stomatocyte. Additional cryo-ET data are provided in the Supporting Information (Figures S15–S16 and Video S1). (e) Schematic illustration of GSH-induced disulfide bond cleavage. (f) Hydrodynamic diameter of GSH-stomatocytes before and after treatment with 10 mM glutathione (GSH). (g) SEM images showing the morphology of GSH-stomatocytes before and after incubation with 10 mM GSH for 4 h. (h) MTX release profiles from MTX-stomatocytes and MTX-GSH-stomatocytes in PBS (pH 7.4) at 37°C, in the presence or absence of 10 mM GSH ($n = 3$; data are presented as mean ± SD).

visualize the directed motion of the nanomotors along the H_2O_2 concentration gradient, cyanine5 (Cy5) loaded MnO_2-GSH-stomatocyte nanomotors were employed. Specifically, 1 mM H_2O_2 and the nanomotors were simultaneously introduced into the two chambers of a pre-filled water channel (Figure 3d), allowing an H_2O_2 concentration gradient to form through diffusion. After 15 min of incubation, fluorescence images were captured at the interface region using confocal laser scanning microscopy (CLSM). The CLSM images clearly revealed that the nanomotors migrated along the H_2O_2 concentration gradient. In contrast, no significant fluorescence signal was observed in the negative control groups, confirming the positive chemotactic movement capability of the MnO_2-GSH-stomatocyte nanomotors (Figure 3d).

Encouraged by the motility of the nanomotors, we next investigated their cargo delivery efficiency and therapeutic performance in vitro. The cytotoxicity of MnO_2-GSH-stomatocytes was first evaluated using a standard Cell Counting Kit-8 (CCK-8) assay prior to cellular studies. RAW 264.7 macrophage cells were used as the model system. As shown in Figure S17, the MnO_2-GSH-stomatocytes exhibited negligible cytotoxicity, maintaining over 90% cell viability even at concentrations up to 400 μg/mL. The cellular uptake of MnO_2-GSH-stomatocytes was then examined

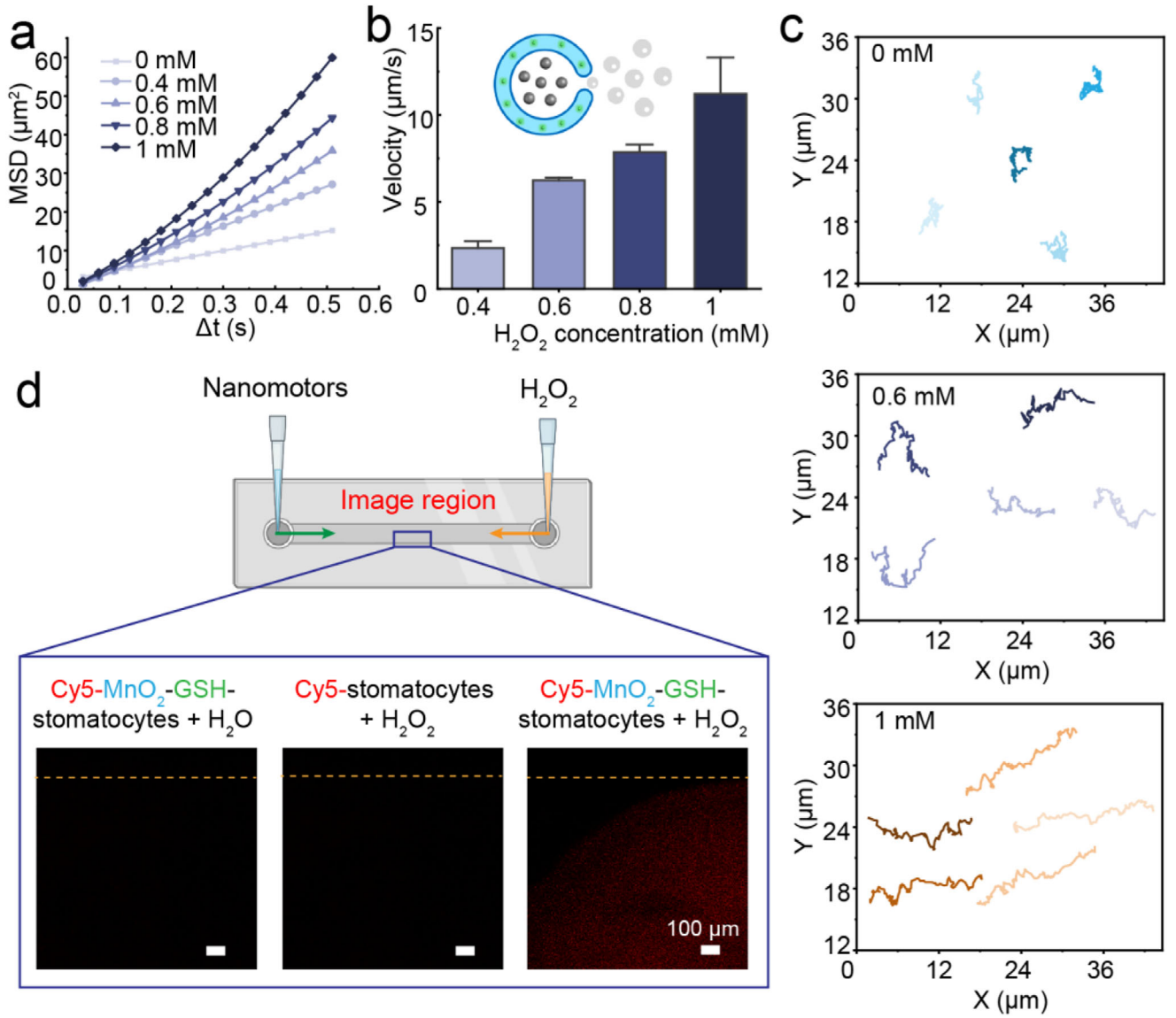

FIGURE 3 | Motion behavior of MnO_2-GSH-stomatocytes. (a) Mean square displacement (MSD) curves of MnO_2-GSH-stomatocytes as a function of H_2O_2 concentration (0, 0.4, 0.6, 0.8, and 1 mM). (b) Velocities of MnO_2-GSH-stomatocytes as a function of H_2O_2 concentration. Velocities were theoretically calculated by fitting the MSD curves according to the equation MSD = $(4D)\Delta t + (V^2)(\Delta t^2)$ and are presented as mean ± SD [29]. (c) Representative motion trajectories of MnO_2-GSH-stomatocytes under varying H_2O_2 concentrations. (d) Schematic illustration of the experimental setup for chemotactic motion analysis in a single microfluidic channel, achieved by the simultaneous introduction of fuel (H_2O_2) and nanomotors (MnO_2 loaded Cy5 labeled GSH-stomatocytes). Corresponding fluorescence images show the chemotactic migration behavior of MnO_2-GSH-stomatocytes. Scale bar = 100 μm.

in both non-activated and lipopolysaccharide (LPS)-activated RAW 264.7 cells using Cy5-labeled stomatocytes and CLSM. To establish an in vitro inflammatory macrophage model that mimics the osteoarthritic microenvironment, LPS was employed, as it activates Toll-like receptors in RAW 264.7 cells, thereby triggering downstream signaling pathways, specifically NF-κB and MAPKs (ERK, JNK, and p38). This activation leads to a robust release of pro-inflammatory cytokines, including TNF-α, IL-6, and IL-1β. Furthermore, it induces an inflammatory response, enhances phagocytic activity, and results in characteristic morphological changes in macrophages. As shown in Figure 4a, a significantly stronger red fluorescence signal was observed in LPS-activated RAW264.7 cells compared to the non-activated control group. This enhanced uptake is attributed to the self-propelled motion of the MnO_2-GSH-stomatocyte nanomotors in the H_2O_2-enriched inflammatory environment (Figure S18). Quantitative fluorescence analysis further confirmed that the intracellular fluorescence intensity of nanomotor-treated LPS-activated cells was 1.7-fold and 2.6-fold higher than that of empty stomatocytes-treated LPS-activated cells and nanomotor-treated non-activated cells, respectively (Figure 4c). These results demonstrate that the active motion of MnO_2-GSH-stomatocyte nanomotors significantly enhances their cellular uptake, suggesting improved therapeutic potential in inflammatory conditions.

Reactive oxygen species (ROS) play a critical role in cartilage degradation and chondrocyte apoptosis, which are key effects of OA. Excessive accumulation of H_2O_2 can cause severe cellular

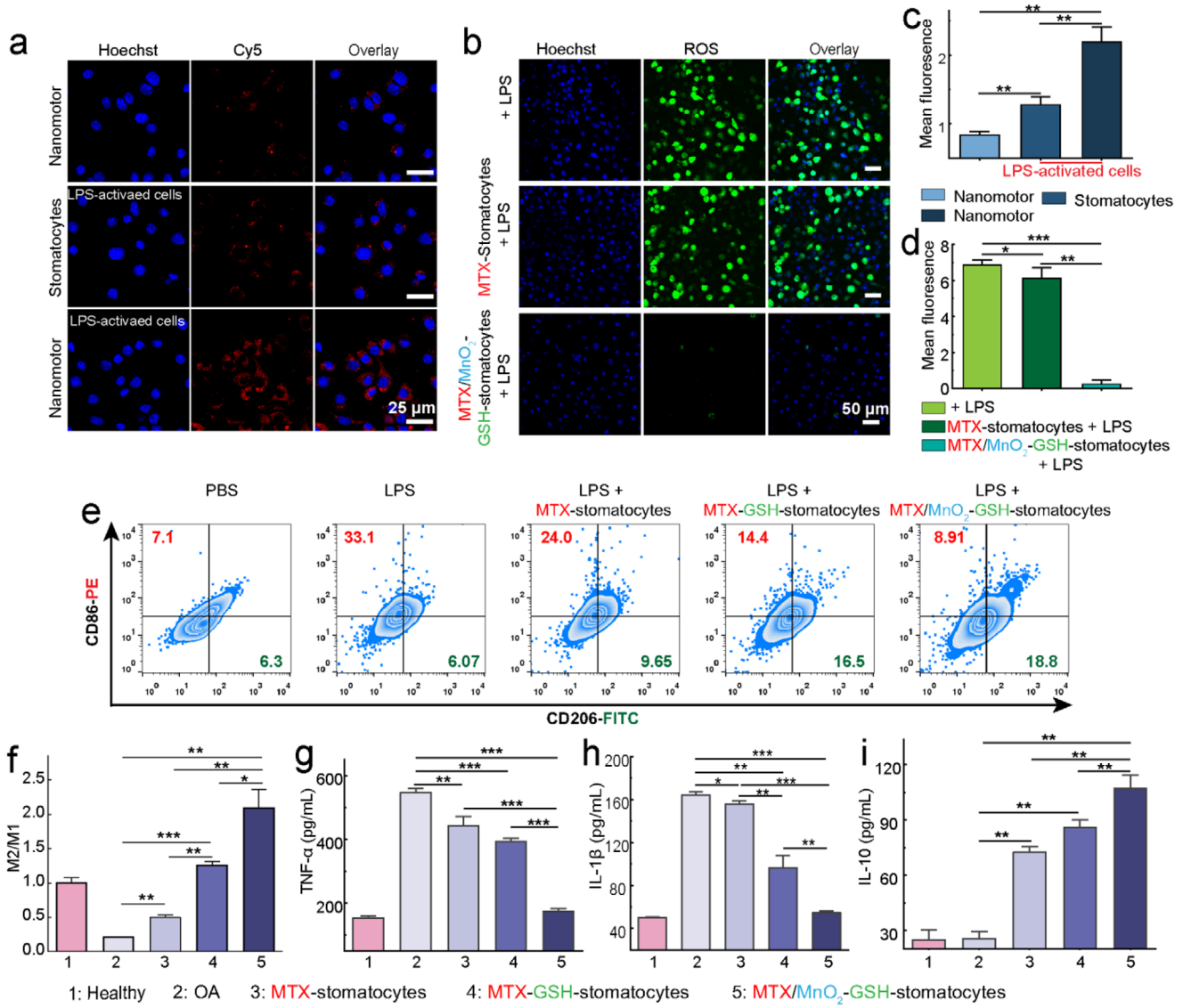

FIGURE 4 | In vitro cellular uptake, ROS scavenging, macrophage M2 phenotype polarization, and anti-inflammatory cytokine secretion. (a) Confocal laser scanning microscopy (CLSM) single slice images of LPS-activated or non-activated RAW 264.7 cells after 8 h incubation with Cy5-nanomotor (Cy5-MnO_2-GSH-stomatocytes) and Cy5-stomatocytes, respectively. Scale bar = 25 μm. (b) Intracellular ROS levels in RAW 264.7 cells following 12 h treatment with MTX/MnO_2-GSH-stomatocytes and MTX-stomatocytes. Scale bar = 50 μm. (c) Quantitative analysis of Cy5 mean fluorescence intensity measured using ImageJ ($n = 3$; data presented as mean ± SD). (d) Quantitative analysis of ROS mean fluorescence intensity measured using ImageJ ($n = 3$; data presented as mean ± SD). (e) Representative flow cytometry plots showing CD86 and CD206 expression in LPS-activated RAW 264.7 cells after 24 h treatment with different stomatocyte formulations. (f) Quantification of M2/M1 macrophage ratios in RAW 264.7 cells from different treatment groups determined by flow cytometry ($n = 3$; data presented as mean ± SD). (g-i) ELISA analysis of TNF-α (g), IL-1β (h), and IL-10 (i) secretion from LPS-activated RAW 264.7 cells after 24 h treatment with MTX-stomatocytes, MTX-GSH-stomatocytes, or MTX/MnO_2-GSH-stomatocytes ($n = 3$; data presented as mean ± SD). Statistical significance in (c-d) and (f-i) was determined by one-way analysis of variance (ANOVA) using IBM SPSS Statistic 25 software. * $p < 0.05$; ** $p < 0.01$; *** $p < 0.001$.

and tissue damage, thereby amplifying oxidative stress and inflammation. To evaluate intracellular ROS levels, ROS probe of 2',7'-dichlorofluorescein diacetate (DCFH-DA) was employed as a ROS-sensitive probe and its fluorescence after oxidation was visualized by CLSM. As shown in Figure 4b–d, the LPS-activated group exhibited a markedly increased fluorescent signal, indicating elevated ROS production. In contrast, cells treated with the nanomotors displayed the lowest ROS levels, which can be attributed to the synergistic action of MTX-mediated anti-inflammatory activity and H_2O_2 decomposition by MnO_2 NPs, thereby alleviating the local hypoxic environment.

Macrophage polarization from the pro-inflammatory M1 phenotype to the anti-inflammatory M2 phenotype serves as an important indicator of therapeutic efficacy. To examine this effect, the polarization ability of the MTX/MnO_2-GSH-stomatocyte nanomotors was assessed by flow cytometry, analyzing the expression levels of CD86 (M1 marker) and CD206 (M2 marker).

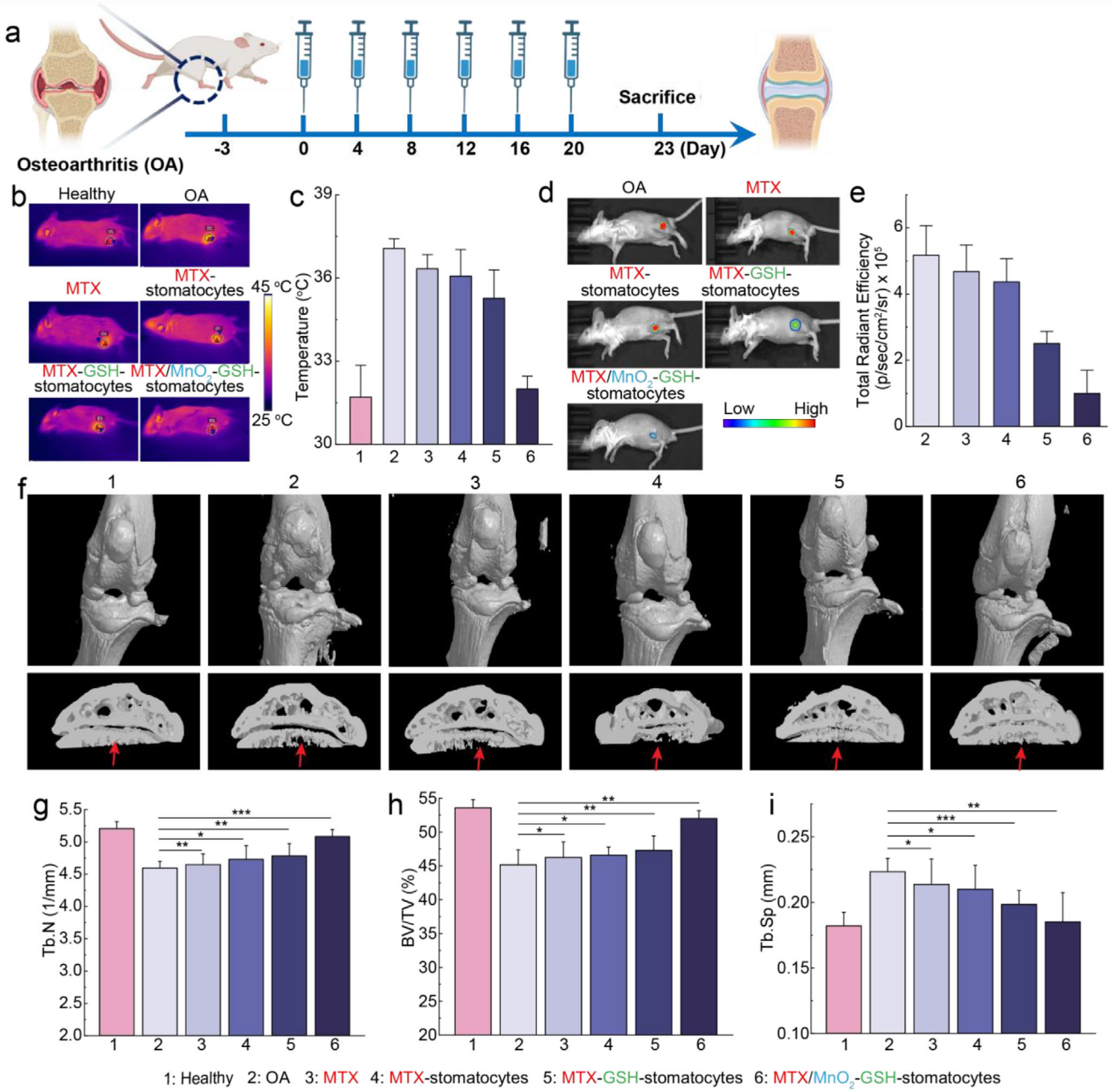

FIGURE 5 | In vivo therapeutic evaluation of the MTX/MnO_2-GSH-stomatocyte nanomotors. (a) Schematic illustration of the treatment plan for the OA mouse model. (b) Representative thermographic images of healthy and arthritic knees following different treatments ($n = 5$). (c) Quantification of knee temperature in healthy and OA mice after various treatments ($n = 5$; data presented as mean ± SD). (d) Representative in vivo fluorescence images showing ROS scavenging effects of free MTX, MTX-stomatocytes, MTX-GSH-stomatocytes, and MTX/MnO_2-GSH-stomatocytes ($n = 5$). (e) Corresponding quantification of fluorescence intensity ($n = 5$; data presented as mean ± SD). (f) Representative micro-CT images of knee joints in healthy and OA mice after different treatments ($n = 5$). (g) Quantitative analyses of trabecular number (Tb.N). (h) Quantitative analyses of bone volume fraction (BV/TV). (i) Quantitative analyses of trabecular separation (Tb.Sp) in subchondral bone across different groups ($n = 5$; data presented as mean ± SD). Statistical significance in (c, e, and g-i) were calculated via a one-way analysis of variance (ANOVA) with IBM SPSS Statistic 25 software. * $p < 0.05$; ** $p < 0.01$; *** $p < 0.001$.

As shown in Figure 4e, macrophages treated with the nanomotors exhibited higher CD206 and lower CD86 expression compared with the control groups, demonstrating a pronounced shift toward the M2 phenotype. This effect is primarily ascribed to the enhanced cellular uptake and rapid MTX release enabled by the self-propelled nanomotors. Consistently, the M2/M1 ratio for the nanomotor-treated group was significantly higher than that of the MnO_2/MTX-stomatocytes and MTX-GSH-stomatocytes groups (Figure 4f). Furthermore, the expression levels of pro-inflammatory cytokines (TNF-α and IL-1β) and anti-inflammatory cytokines (IL-10) were quantified using ELISA (Figure 4g–i). Cells treated with MTX/MnO_2-GSH-stomatocyte nanomotors showed markedly decreased TNF-α and IL-1β secretion [46], accompanied by elevated IL-10 expression, compared

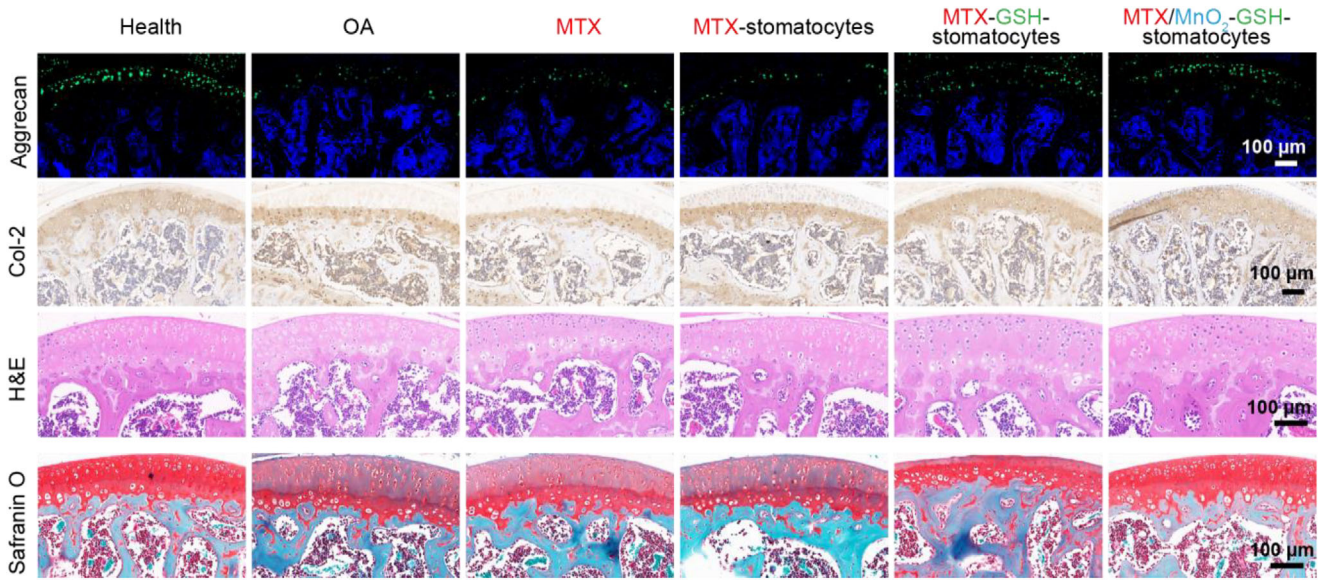

FIGURE 6 | Evaluation of pathological features following different treatments. Representative images of aggrecan, collagen II (Col-2), hematoxylin-eosin (H&E), and safranin O staining of knee joints from healthy and osteoarthritic (OA) mice after various treatments. Scale bar = 100 μm.

with control groups. These results confirm that the MTX/MnO_2-GSH-stomatocyte nanomotors effectively suppress inflammatory responses, owing to their self-propelled motion that enhances targeted cellular interaction, and responsive MTX release which improves therapeutic efficacy.

Having demonstrated enhanced cellular uptake efficiency and in vitro therapeutic effect of the nanomotors, we further conducted in vivo experiments using a monoiodoacetate (MIA)-induced osteoarthritis (OA) mouse model. First, the in vivo biosafety of the MTX/MnO_2-GSH-stomatocyte nanomotors was evaluated through serum biochemical analysis (n = 5 per group). Comprehensive blood biochemical assessments revealed that all measured parameters in mice treated with MTX/MnO_2-GSH-stomatocyte nanomotors remained within normal safety ranges (Figure S19), confirming the absence of significant adverse effects. To construct an OA mouse model, eight-week-old mice were anesthetized and injected with MIA into the knee joint to induce OA over an 8-day period. Subsequently, OA mice were intra-articularly injected into the knee joints every 4 days with PBS, free MTX, MTX-stomatocytes, MTX-GSH-stomatocytes, and MTX/MnO_2-GSH-stomatocytes, while healthy mice injected with PBS served as controls (Figures 5a and S20) (n = 5 per group). A characteristic feature of inflammation is elevated joint temperature caused by synovitis-induced hyperthermia [47]. Therefore, knee joint temperature changes were recorded using a FLIR infrared thermal camera following the various treatments (n = 5 per group). As shown in Figure 5b,c, the knee joint temperatures in all treated groups were lower than those in the untreated OA group, indicating effective suppression of inflammation. Notably, the temperature in the nanomotor-treated group was markedly lower than that of the other treatment groups and comparable to that of healthy mice, suggesting improved therapeutic efficacy of the nanomotors. To further elucidate the therapeutic effect of MTX/MnO_2-GSH-stomatocyte nanomotors in OA mice, we examined the in vivo ROS levels. A reduction in ROS levels within OA joints alleviates oxidative stress and inflammation, thereby supporting the enhanced therapeutic efficacy of the treatment. The luminescence probe L-012 was administered into the joints of mice, and the distribution of ROS was monitored using an in vivo imaging system (n = 5 per group). As shown in Figure 5d,e, compared with the PBS, free MTX, MTX-stomatocytes, and MTX-GSH-stomatocytes groups, the MTX/MnO_2-GSH-stomatocyte nanomotors group exhibited the weakest joint luminescence and lowest luminescence intensity, indicating its superior ability to scavenge ROS. To further investigate potential organ toxicity, resulting from stomatocyte accumulation, hematoxylin-eosin (H&E) staining was performed on slices of major organs, including the heart, liver, spleen, lungs, and kidneys (n = 5 per group). As shown in Figure S21, histopathological examination revealed no apparent abnormalities or lesions in any of these organs following treatment with the various nanoparticle formulations, confirming that the developed nanomaterials do not induce organ toxicity. Collectively, these findings demonstrate that MTX/MnO_2-GSH-stomatocyte nanomotors exhibit a good biosafety profile after intra-articular administration.

After treatments, the knee joints were harvested, and the bone morphology and microstructural characteristics of the subchondral bone were analyzed by micro-CT imaging to further evaluate the therapeutic outcomes (Figure 5f). Histomorphometry analysis of CT images was performed to evaluate bone structure indices, including trabecular number (Tb.N), trabecular separation (Tb.Sp), and bone volume fraction (BV/TV). The control group exhibited severe bone and cartilage erosion, characterized by a significant increase in Tb.Sp. and a decrease in BV/TV and Tb.N, confirming suppressed osteosynthesis (Figure 5g–i). In contrast, the treatment groups—free MTX, MTX-stomatocytes, MTX-GSH-stomatocytes, and MTX/MnO_2-GSH-stomatocytes—showed attenuated articular cartilage degeneration. Notably, the MTX/MnO_2-GSH-stomatocytes group displayed no pathological alterations in the articular cartilage and demonstrated lower Tb.Sp alongside higher BV/TV and Tb.N compared to the

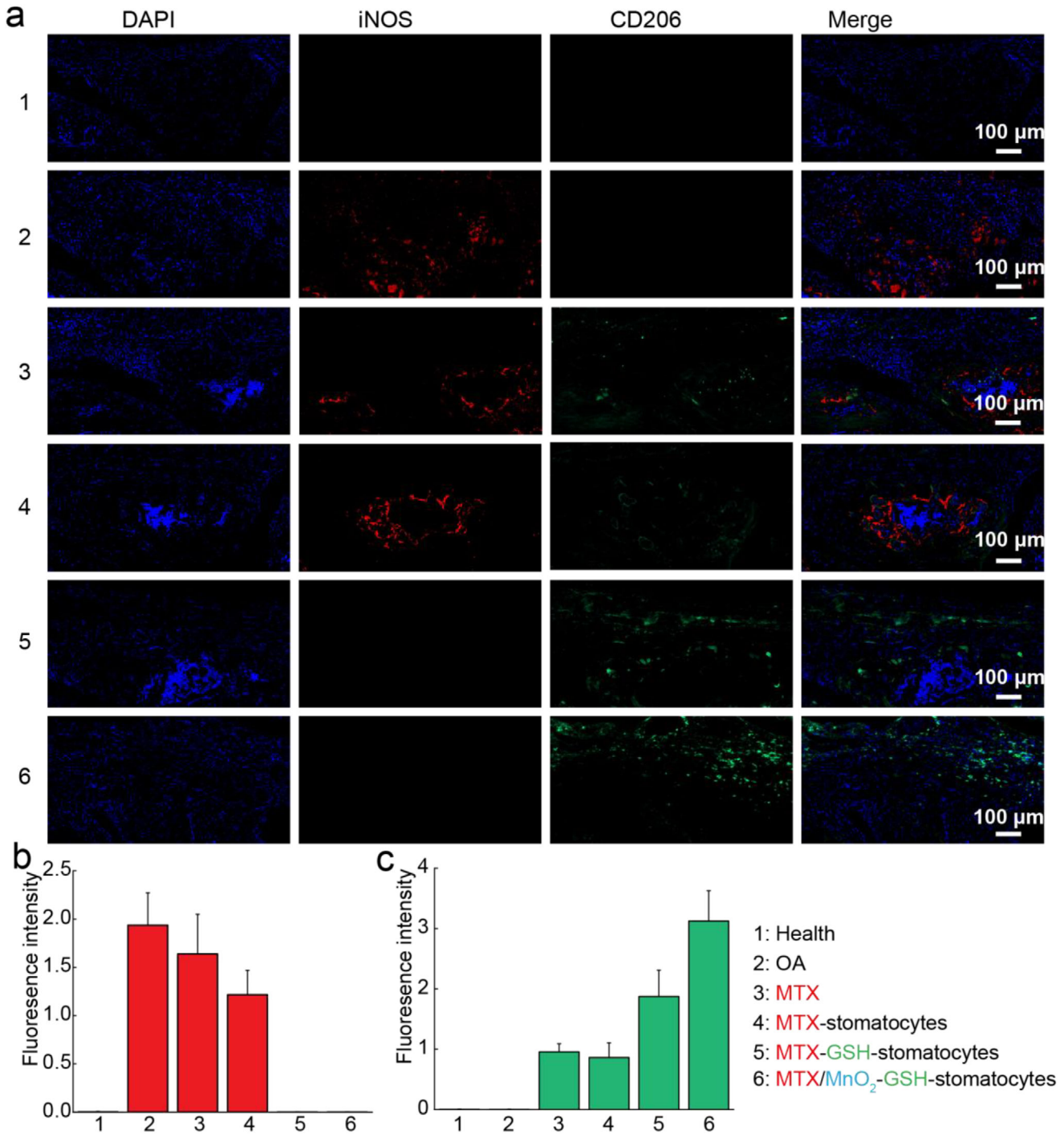

FIGURE 7 | Immunofluorescence staining of protein markers CD206 and iNOS in the synovial region (a), and the corresponding fluorescence intensities of CD206 (b), and iNOS (c) quantified using ImageJ ($n = 5$, data are presented as mean ± SD). Scale bar = 100 μm.

passive stomatocytes groups, confirming its enhanced efficacy in preventing bone degradation.

Extracellular matrix (ECM) degradation in mouse joints is a key factor contributing to articular cartilage destruction, characterized by the loss of proteoglycans, collagen type X, and aggrecan. To assess the therapeutic efficacy of MTX/MnO_2-GSH-stomatocyte nanomotors, immunohistochemical analyses were performed to evaluate ECM integrity. H&E, safranin O, and aggrecan stainings were used for the histological assessment of cartilage sections after treatment. As shown in Figure 6, compared with the healthy group, the untreated OA group exhibited pronounced degenerative changes in cartilage. In contrast, the treatment groups (free MTX, MTX-stomatocytes, MTX-GSH-stomatocytes, and MTX/MnO_2-GSH-stomatocytes nanomotors) yielded varying degrees of therapeutic improvement. Among them, the MTX/MnO_2-GSH-stomatocytes nanomotors group displayed a significantly improved therapeutic outcome, with smooth and ordered cartilage surface, and aggrecan (immunofluorescence staining) and proteoglycans (safranin O staining)

strongly distributed in the articular cartilage, quite similar to the healthy group. The M2 macrophage polarization capacity of MTX/MnO_2-GSH-stomatocyte nanomotors was further proven by immunofluorescence staining (typical markers of macrophage phenotype: iNOS and CD206 protein) of synovium macrophage after OA treatment. As shown in Figure 7a–c, in comparison to the control groups, the lowest red fluorescence signals of iNOS and highest green fluorescence signals of CD206 were monitored in the group of MTX/MnO_2-GSH-stomatocyte nanomotors, suggesting that they could induce M2 macrophage polarization to exert their treatment effect on synovitis.

3 | Conclusion

In summary, we have successfully developed a chemically driven GSH-responsive stomatocyte nanomotor by incorporating a disulfide linker into the stomatocyte framework and by in situ encapsulating MnO_2 NPs within its nanocavity. Under inflammatory microenvironmental conditions, these nanomotors exhibited excellent self-propelled motion driven by concentration gradients generated through O_2 release from the nanocavity and the concurrent consumption of H_2O_2 in OA tissue. The generated O_2 not only powered the nanomotor's motion but also helped alleviate the hypoxic and inflammatory environment associated with OA. Moreover, the GSH levels in OA triggered the sustained release of MTX. Both in vitro (2D cell models, established via LPS-induced pro-inflammatory cytokine release in RAW 264.7 cells) and in vivo (tumor-bearing mice) evaluations confirmed enhanced nanomotor accumulation and therapeutic efficacy, with no significant side effects observed.

Author Contributions

Jianhong Wang: conceptualization, investigation, writing – original draft, methodology, writing – review and editing. **Mengsi Zhan**: methodology, writing – review and editing, data curation. **Hanglong Wu**: investigation, methodology, formal analysis, writing – review and editing. **Maarten Bransen**: investigation, writing – review and editing, formal analysis, data curation. **Ioanna Balmpouzi**: investigation, data curation. **Xianwen Lou**: formal analysis, data curation. **Junjie Liu**: investigation, data curation. **Nina Wang**: investigation, data curation. **Zhiqiang Wang**: investigation, data curation. **Heiner Friedrich**: formal analysis, writing – review and editing. **Jingxin Shao**: conceptualization, investigation, formal analysis, data curation, writing – original draft, writing – review and editing, supervision. **Jan C. M. van Hest**: conceptualization, funding acquisition, writing – review & editing, formal analysis, supervision. **Xiangyang Shi**: conceptualization, funding acquisition, writing – review and editing, supervision, formal analysis.

Acknowledgments

This study was financially supported by The Netherlands Ministry of Education, Culture and Science (Gravitation Program Interactive Polymer Materials 024.005.020, Gravitation Program Materials Driven Regeneration 024.003.013 and the Spinoza premium SPI 72–259), the National Natural Science Foundation of China (52350710203, U23A2096, and W2421104), the Science and Technology Commission of Shanghai Municipality (23520712500 and 20DZ2254900), and the China-Central and Eastern European Countries (CEEC) Joint Education Project (2023256). Funding was also provided by the European Union (ERC, PRO-ARTIS, 101141866). Views and opinions expressed are however those of the author(s) only and do not necessarily reflect those of the European Union or the European Research Council. Neither the European Union nor the granting authority can be held responsible for them. Schematic illustrations (e.g., mice, cells, osteoarthritis knee, and syringe) were created with BioRender.com.

Conflicts of Interest

The authors declare no conflicts of interest.

Data Availability Statement

The data that support the findings of this study are available from the corresponding author upon reasonable request.

References

1. T. P. Padial, S. Chen, A. C. Hortelão, A. Sen, and S. Sánchez, "Swarming Intelligence in Self-propelled Micromotors and Nanomotors," *Nature Reviews Materials* 10 (2025), 947–963, https://doi.org/10.1038/s41578-025-00818-x.

2. S. Chen, D. E. Fan, P. Fischer, et al., "A Roadmap for Next-generation Nanomotors," *Nature Nanotechnology* 20 (2025): 990–1000, https://doi.org/10.1038/s41565-025-01962-9.

3. A. D. Fusi, Y. Li, A. Llopis-Lorente, T. Patiño, J. C. M. van Hest, and L. K. E. A. Abdelmohsen, "Achieving Control in Micro-/Nanomotor Mobility," *Angewandte Chemie International Edition* 62 (2023): e202214754, https://doi.org/10.1002/anie.202214754.

4. H. Choi, S. Jeong, C. Simó, et al., "Urease-powered Nanomotor Containing STING Agonist for Bladder Cancer Immunotherapy," *Nature Communications* 15 (2024): 9934, https://doi.org/10.1038/s41467-024-54293-z.

5. L. Tao, Y. Wu, M. Mao, W. Lu, and Q. He, "Inflammatory-Directed Nanomotors for Targeted Osteoarthritis Treatment," *Advanced Healthcare Material* 14 (2025): e01206, https://doi.org/10.1002/adhm.202501206.

6. Z. Gao, Z. Yang, M. Luo, et al., "Trienzyme-in-One Nanoparticle Making Multifunctional Synergistic Nanorobot for Tumor Therapy," *Small Methods* 9 (2025): 2500142, https://doi.org/10.1002/smtd.202500142.

7. M. Xuan, Z. Wu, J. Shao, L. Dai, T. Si, and Q. He, "Near Infrared Light-Powered Janus Mesoporous Silica Nanoparticle Motors," *Journal of the American Chemical Society* 138 (2016): 6492–6497, https://doi.org/10.1021/jacs.6b00902.

8. S. Cao, J. Shao, H. Wu, et al., "Photoactivated Nanomotors via Aggregation Induced Emission for Enhanced Phototherapy," *Nature Communications* 12 (2021): 2077.

9. J. Wang, Z. Xiong, J. Zheng, X. Zhan, and J. Tang, "Light-Driven Micro/Nanomotor for Promising Biomedical Tools: Principle, Challenge, and Prospect," *Accounts of Chemical Research* 51 (2018): 1957–1965, https://doi.org/10.1021/acs.accounts.8b00254.

10. Y. Shen, W. Zhang, G. Li, et al., "Adaptive Control of Nanomotor Swarms for Magnetic-Field-Programmed Cancer Cell Destruction," *ACS Nano* 15 (2021): 20020–20031, https://doi.org/10.1021/acsnano.1c07615.

11. W. Li, C. Wu, Z. Xiong, et al., "Self-driven Magnetorobots for Recyclable and Scalable Micro/Nanoplastic Removal From Nonmarine Waters," *Science Advances* 8 (2022): eade1731, https://doi.org/10.1126/sciadv.ade1731.

12. F. Chen, D. Jin, Y. Song, et al., "Magnetically Powered Heterogeneous Swarm as Controllable Immunosorbent Probes for Active Motion-Enhanced Photoinitiated Chemiluminescence Detection," *Advanced Functional Materials* 35 (2025): 2504395, https://doi.org/10.1002/adfm.202504395.

13. M. Ding, B. Chen, D. A. Wilson, Y. Tu, and F. Peng, "From Autonomous Chemical Micro-/Nanomotors to Rationally Engineered Bio-Interfaces," *Angewandte Chemie International Edition* 64 (2025): e202423207, https://doi.org/10.1002/anie.202423207.

14. S. Sánchez, L. Soler, and J. Katuri, "Chemically Powered Micro- and Nanomotors," *Angewandte Chemie International Edition* 54 (2015): 1414–1444, https://doi.org/10.1002/anie.201406096.

15. M. Chung, W. Chia, W. Wan, Y. Lin, and H. Sung, "Controlled Release of an Anti-inflammatory Drug Using an Ultrasensitive ROS-Responsive Gas-Generating Carrier for Localized Inflammation Inhibition," *Journal of the American Chemical Society* 137 (2015): 12462–12465, https://doi.org/10.1021/jacs.5b08057.

16. M. López-Lázaro, "Dual Role of Hydrogen Peroxide in Cancer: Possible Relevance to Cancer Chemoprevention and Therapy," *Cancer Letters* 252 (2007): 1–8, https://doi.org/10.1016/j.canlet.2006.10.029.

17. C. Simó, M. Serra-Casablancas, A. C. Hortelao, et al., "Urease-Powered Nanobots for Radionuclide Bladder Cancer Therapy," *Nature Nanotechnology* 19 (2024): 554–564.

18. J. Jiang, H. Liang, Y. Ye, et al., "Stem Cell Secretome Armed Magneto-actuated Micromotors as Spatio-temporal Manipulators for Wound Healing Acceleration," *Nature Communications* 16 (2025): 6754, https://doi.org/10.1038/s41467-025-61914-8.

19. S. Zhao, K. Gao, H. Han, et al., "Acid-degradable Lipid Nanoparticles Enhance the Delivery of mRNA," *Nature Nanotechnology* 19 (2024): 1702–1711, https://doi.org/10.1038/s41565-024-01765-4.

20. I. A. B. Pijpers, L. K. E. A. Abdelmohsen, D. S. Williams, and J. C. M. van Hest, "Morphology under Control: Engineering Biodegradable Stomatocytes," *ACS Macro Letters* 6 (2017): 1217–1222, https://doi.org/10.1021/acsmacrolett.7b00723.

21. P. A. Wong, "A Basis of Echinocytosis and Stomatocytosis in the Disc–Sphere Transformations of the Erythrocyte," *Journal of Theoretical Biology* 196 (1999): 343–361, https://doi.org/10.1006/jtbi.1998.0845.

22. K. T. Kim, J. Zhu, S. A. Meeuwissen, et al., "Polymersome Stomatocytes: Controlled Shape Transformation in Polymer Vesicles," *Journal of the American Chemical Society* 132 (2010): 12522–12524, https://doi.org/10.1021/ja104154t.

23. L. K. E. A. Abdelmohsen, M. Nijemeisland, G. M. Pawar, et al., "Dynamic Loading and Unloading of Proteins in Polymeric Stomatocytes: Formation of an Enzyme-Loaded Supramolecular Nanomotor," *ACS Nano* 10, no. 2 (2016): 2652–2660, https://doi.org/10.1021/acsnano.5b07689.

24. M. Nijemeisland, L. K. E. A. Abdelmohsen, W. T. S. Huck, D. A. Wilson, and J. C. M. van Hest, "A Compartmentalized Out-of-Equilibrium Enzymatic Reaction Network for Sustained Autonomous Movement," *ACS Central Science* 2, no. 11 (2016): 843–849, https://doi.org/10.1021/acscentsci.6b00254.

25. H. Che, J. Zhu, S. Song, et al., "ATP-Mediated Transient Behavior of Stomatocyte Nanosystems," *Angewandte Chemie International Edition* 131 (2019): 13247–13252, https://doi.org/10.1002/ange.201906331.

26. A. C. Wauters, J. F. Scheerstra, M. M. T. van Leent, et al., "Polymersomes with Splenic Avidity Target Red Pulp Myeloid Cells for Cancer Immunotherapy," *Nature Nanotechnology* 19 (2024): 1735–1744, https://doi.org/10.1038/s41565-024-01727-w.

27. Y. Liu, R. Terracciano, J. Scheerstra, et al., "Fast and Autonomous Mannosylated Nanomotors for Dynamic Cancer Cell Targeting," *Angewandte Chemie International Edition* 64 (2025): e202505717, https://doi.org/10.1002/anie.202505717.

28. J. Wang, H. Wu, X. Zhu, et al., "Ultrafast Light-Activated Polymeric Nanomotors," *Nature Communications* 15 (2024): 4878, https://doi.org/10.1038/s41467-024-49217-w.

29. I. A. B. Pijpers, S. Cao, A. Llopis-Lorente, et al., "Hybrid Biodegradable Nanomotors Through Compartmentalized Synthesis," *Nano Letters* 20 (2020): 4472–4480, https://doi.org/10.1021/acs.nanolett.0c01268.

30. J. Wang, A. Polyviou, J. F. Scheerstra, et al., "Dual-driven Biodegradable Nanomotors for Enhanced Cellular Uptake," *Journal Material Chemical B* 13 (2025): 2820–2825, https://doi.org/10.1039/D4TB02633K.

31. Y. Guo, J. Wang, G. Li, et al., "Oxygen and Heat Dual-Driven Stomatocyte Nanomotors for Highly Efficient Inflammation-Relieved Breast Tumor Photothermal Therapy," *Advanced Functional Materials* 35 (2025): 2500113, https://doi.org/10.1002/adfm.202500113.

32. R. Bej, K. Achazi, R. Haag, and S. Ghosh, "Polymersome Formation by Amphiphilic Polyglycerol- b -polydisulfide- b -polyglycerol and Glutathione-Triggered Intracellular Drug Delivery," *Biomacromolecules* 21 (2020): 3353–3363, https://doi.org/10.1021/acs.biomac.0c00775.

33. S. Bera and S. Ghosh, "Alternating vs. random Amphiphilic Polydisulfides: Aggregation, Enzyme Activity Inhibition and Redox-responsive Guest Release," *Nanoscale* 16 (2024): 17886–17892, https://doi.org/10.1039/D4NR02494J.

34. D. Braatz, M. Cherri, M. Tully, et al., "Chemical Approaches to Synthetic Drug Delivery Systems for Systemic Applications," *Angewandte Chemie International Edition* 61 (2022): e202203942, https://doi.org/10.1002/anie.202203942.

35. G. Ma, D. Braatz, P. Tang, et al., "Polyglycerol-Shelled Reduction-Sensitive Polymersome for DM1 Delivery to HER-2-Positive Breast Cancer," *Biomacromolecules* 25 (2024): 4440–4448, https://doi.org/10.1021/acs.biomac.4c00512.

36. J. Shao, S. Cao, D. S. Williams, L. K. E. A. Abdelmohsen, and J. C. M. van Hest, "Photoactivated Polymersome Nanomotors: Traversing Biological Barriers," *Angewandte Chemie International Edition* 59 (2020): 16918–16925, https://doi.org/10.1002/anie.202003748.

37. Y. Tu, F. Peng, P. B. White, and D. A. Wilson, "Redox-Sensitive Stomatocyte Nanomotors: Destruction and Drug Release in the Presence of Glutathione," *Angewandte Chemie International Edition* 56 (2017): 7620–7624, https://doi.org/10.1002/anie.201703276.

38. X. Hu, Y. Zhang, Z. Xie, X. Jing, A. Bellotti, and Z. Gu, "Stimuli-Responsive Polymersomes for Biomedical Applications," *Biomacromolecules* 18 (2017): 649–673, https://doi.org/10.1021/acs.biomac.6b01704.

39. A. Homma, H. Sato, T. Tamura, et al., "Synthesis and Optimization of Hyaluronic Acid–methotrexate Conjugates to Maximize Benefit in the Treatment of Osteoarthritis," *Bioorganic & Medicinal Chemistry* 18 (2010): 1062–1075, https://doi.org/10.1016/j.bmc.2009.12.053.

40. Y. Wang, G. Jones, H. I. Keen, et al., "Methotrexate to Treat Hand Osteoarthritis With Synovitis (METHODS): An Australian, Multisite, Parallel-group, Double-blind, Randomised, Placebo-controlled Trial," *Lancet* 402 (2023): 1764–1772, https://doi.org/10.1016/S0140-6736(23)01572-6.

41. M. Zhan, H. Sun, Z. Wang, et al., "Nanoparticle-Mediated Multiple Modulation of Bone Microenvironment to Tackle Osteoarthritis," *ACS Nano* 18 (2024): 10625–10641, https://doi.org/10.1021/acsnano.4c00909.

42. L. K. E. A. Abdelmohsen, D. S. Williams, J. Pille, et al., "Formation of Well-Defined, Functional Nanotubes via Osmotically Induced Shape Transformation of Biodegradable Polymersomes," *Journal of the American Chemical Society* 138 (2016): 9353–9356, https://doi.org/10.1021/jacs.6b03984.

43. S. Song, H. Han, J. Wang, et al., "Polymersome-based Nanomotors: Preparation, Motion Control, and Biomedical Applications," *Chemical Science* 16 (2025): 7106–7129, https://doi.org/10.1039/D4SC08283D.

44. D. A. Wilson, R. J. M. Nolte, and J. C. M. van Hest, "Entrapment of Metal Nanoparticles in Polymer Stomatocytes," *Journal of the American Chemical Society* 134 (2012): 9894–9897, https://doi.org/10.1021/ja3029872.

45. H. Wu, T. Li, S. P. Maddala, et al., "Studying Reaction Mechanisms in Solution Using a Distributed Electron Microscopy Method," *ACS Nano* 15 (2021): 10296–10308, https://doi.org/10.1021/acsnano.1c02461.

46. C. Chen, Q. Wei, Z. Zhu, et al., "A Thermoresponsive Magnetic Nanocarrier With the DNA-mimetic Base Pairing-guided Controlled Release of Methotrexate in the Treatment of Rheumatoid Arthritis," *Journal Control Release* 384 (2025): 113952, https://doi.org/10.1016/j.jconrel.2025.113952.

47. J. Kim, H. Kim, S. Y. Song, et al., "Synergistic Oxygen Generation and Reactive Oxygen Species Scavenging by Manganese Ferrite/Ceria Co-decorated Nanoparticles for Rheumatoid Arthritis Treatment," *ACS Nano* 13 (2019): 3206–3217, https://doi.org/10.1021/acsnano.8b08785.

Supporting Information

Additional supporting information can be found online in the Supporting Information section.

Supporting File 1: The authors have cited additional references within the Supporting Information.

Supporting File 2: anie72340-sup-0002-Video S1.avi.